Journal of
Materials Chemistry C
Materials for optical, magnetic and electronic devices

This article can be cited before page numbers have been issued, to do this please use: X. Shen, X. Wang, J. Wang, R. Wang, Y. Li, F. Bi and X. Bao, *J. Mater. Chem. C*, 2024, DOI: 10.1039/D4TC03192J.

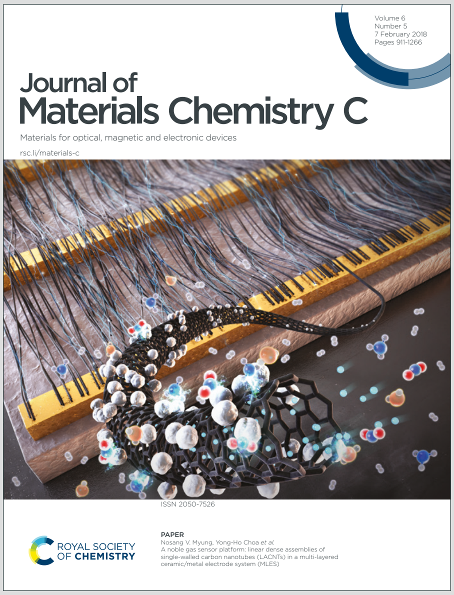

Volume 6
Number 5
7 February 2018
Pages 911-1266

Journal of
Materials Chemistry C
Materials for optical, magnetic and electronic devices
rsc.li/materials-c

ISSN 2050-7526

ROYAL SOCIETY
OF CHEMISTRY

PAPER
Nosang V. Myung, Yong-Ho Choa *et al.*
A noble gas sensor platform: linear dense assemblies of single-walled carbon nanotubes (LACNTs) in a multi-layered ceramic/metal electrode system (MLES)

ROYAL SOCIETY
OF CHEMISTRY

rsc.li/materials-c

View Article Online
DOI: 10.1039/D4TC03192J

Efficient and easily repeatable organic solar cells under high boiling point solvent by introducing highly mixed tolerant guest acceptor

Xiangyu Shen,‡[a,b] Xiaoning Wang,‡[b,c,d] Jianxiao Wang,*[b,c,d] Rulin Wang,*[a] Yonghai Li,[b,c,d] Fuzhen Bi,*[b,c,d] Xichang Bao[b,c,d]

[a] Centre for Theoretical and Computational Physics, College of Physics, Qingdao University, Qingdao 266071, China

[b] Key Laboratory of Photoelectric Conversion and Utilization of Solar Energy, Qingdao Institute of Bioenergy and Bioprocess Technology, Chinese Academy of Sciences
Qingdao 266101, China

[c] Functional Laboratory of Solar Energy, Shandong Energy Institute, Qingdao 266101, China

[d] Qingdao New Energy Shandong Laboratory, Qingdao 266101, China

Abstract

Organic solar cells (OSCs) with low-temperature solution processing have attracted extensive research. To achieve well-phase separation and molecular nucleation crystallization, the active layer usually needs to be processed with low boiling point solvents, which narrows the processing window and limits the implementation of industrial printing processes. Here, we synthesized a novel non fullerene acceptor L8BO-2O as a third component to regulate the performance of the classical PM6:Y6 system in high boiling point solvents. L8BO-2O with an alkoxy chain can effectively suppress the aggregation effect of active materials, which is beneficial for achieving appropriate phase separation in high boiling solvent film-forming processes. Additionally, the similar structure and stacking distance between L8BO-2O and Y6 can effectively improve the mixing tolerance of the host and guest, achieve more effective energy transfer and alloy working mechanisms, thereby greatly increasing light utilization and charge extraction. Finally, the efficiency of the champion ternary OSC reached 16.4% under the doping of 20 wt% L8BO-2O, and the efficiencies of all ternary OSCs were significantly improved under a wide range of doping (0-80 wt%). This result emphasizes the feasibility of introducing a suitable third component to achieve efficient and reproducible OSCs in high boiling point solvents.

View Article Online
DOI: 10.1039/D4TC03192J

Introduction

Organic solar cells (OSCs) have attracted great attention due to their advantages in light-wight, flexibility and semi-transparency.[1-6] With the development of non-fullerene acceptors (NFAs), the power conversion efficiency (PCE) of single junction OSCs has been raised to over 20%.[7-12] Beyond the innovation of donor and acceptor materials, the device fabrication methods also play a critical role in improving device performance. It determines not only the phase separation scale and crystallinity in the macroscope scale but also the intermolecular stacking pattern and stacking distance in the microscopic scale. Only a reasonable combination of active layer materials and fabrication methods can enhance the device performance. Solvent selection is a crucial step during device fabrication.[13, 14] At present, high-performance devices are treated with low-boiling-point chloroform solvents, but in the process of large-area device preparation, it is prone to cause a sharp change in the concentration of active layer materials due to its rapid evaporation rate. An effective solution is to use high-boiling solvents, but the widely-used NFAs tend to excessive aggregation in high-boiling solvents, which seriously limited the improvement of device performance.[14, 15]

The main reason for the excessive aggregation of the NFAs in high boiling solvents is its slow evaporation rate. Several strategies have been proposed to solve this issue and thus optimize the active layer morphology, such as side alkyl chain engineering,[16-20] solvent/solid additives,[21-23] hot-casting strategy[24] and introducing the third component.[25-27] Recently, the ethylene glycol ethyl methyl ether chain was attached to NFAs and the obtained compounds are used as the third component to construct ternary OSCs. The results show this kind of compound can increase the miscibility and crystallinity of the host system, and thus optimize the active layer film-formation kinetics. Finally, the excessive aggregation was effectively suppressed and the obtained device showed enhanced exciton dissociation and charge transportation.[25, 28, 29] Ternary strategy has been widely proven to be a simple and effective way to improve device performance, and ternary OSCs still maintain the highest efficiency of single OSCs.[30-34] However, it is worth noting that the differences in physical and chemical properties between the guest material and the host system in the ternary strategy often result in the crystallinity and morphology of the mixed phase being highly sensitive to component ratios (i.e. low mixing tolerance). The proportion of the guest material to the host generally does not exceed 20 wt%. When a large proportion of the third component is doped, it will cause a sharp decline in device performance. Therefore, in the manufacturing process of

View Article Online
DOI: 10.1039/D4TC03192J

ternary OSCs, precise control of the host to guest ratio is required, which to some extent increases the difficulty of device fabrication. Therefore, solving the problem of excessive aggregation of active layer materials in high boiling solvents and low mixing tolerance of the third component will be the only way to achieve large-scale industrial production.

Hence, we designed and synthesized a novel non-fullerene acceptor L8BO-2O based on polar oligomeric (ethylene glycol) side chains as the third component to regulate the aggregation behavior of the star system PM6:Y6 in the high boiling solvent chlorobenzene (CB). The characteristic polarity oligomeric (ethylene glycol) side chains of L8BO-2O can effectively inhibit the aggregation effect of the active material, increase the miscibility of donors and acceptors, and thus achieve appropriate phase separation in high boiling solvent film-forming processes. The similar structure and stacking distance between L8BO-2O and Y6 can effectively improve the mixing tolerance of the host and guest, achieving effective energy transfer and alloy working mechanism, thereby greatly improving light utilization and charge extraction efficiency. As a result, under a wide doping range of L8BO-2O (0-80 wt% in CB solution), the performance of all ternary OSCs is significantly improved. Both the PCE of PM6:Y6 binary OSCs (14.54%) and PM6:L8BO-2O:Y6 ternary OSCs (16.43%) are at the highest level of the consistent system (Table S1 ESI†). The introduction of the high mixing tolerance third component not only reduces the aggregation of the active materials in high boiling solvents, but also ensures better performance repeatability, which reduces the manufacturing difficulty of the device and lays the foundation for industrial production.

Result and discussion

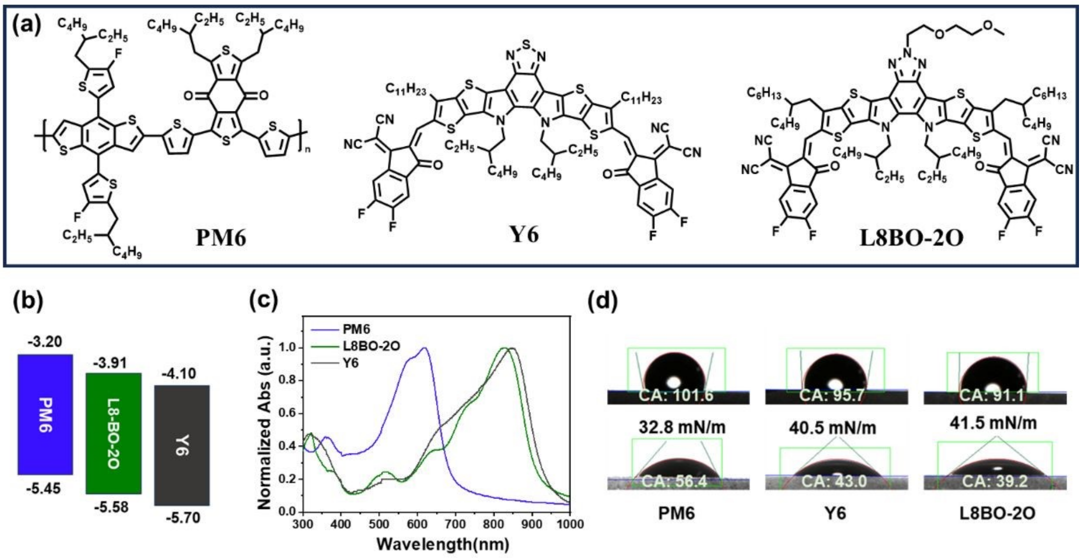

View Article Online
DOI: 10.1039/D4TC03192J

Fig. 1 (a) Chemical structures of donor PM6 and two acceptors Y6, L8BO-2O. (b) Energy levels of PM6, Y6 and L8BO-2O. (c) UV–vis spectra of PM6, Y6 and L8BO-2O neat films. (d) The contact angles of water (top panel) and diiodomethane (bottom panel) droplets on PM6, Y6 and L8BO-2O neat films.

Chemical structures of PM6, Y6 and L8BO-2O are presented in Fig. 1a, and the synthetic routes and detailed characterizations of L8BO-2O are listed in Supporting Information. Subsequently, cyclic voltammetry (C-V) method was used to investigate the energy levels of donor PM6, acceptor Y6 and L8BO-2O, as shown in Fig. S14 (ESI†). A schematic diagram of energy levels is illustrated in Fig. 1b. The lowest unoccupied molecular orbital (LUMO)/highest occupied molecular orbital (HOMO) levels were established to be -3.20/-5.45, -4.10/-5.70, -3.91/-5.58 eV for PM6, Y6 and L8BO-2O, respectively. The LUMO/HOMO of L8BO-2O lie between that of PM6 and Y6, which results in a cascaded energy levels alignment. The cascaded energy level alignment of donor and acceptor can ensure efficient exciton dissociation and charge transport.[35, 36] The normalized UV–vis spectra of PM6, Y6 and L8BO-2O neat films are shown in Fig. 1c. Compared with Y6, the L8BO-2O exhibits a slightly blue shift at the maximum, which form complementary absorption spectra and is beneficial for enhancing photon capture ability of the ternary active layer. In addition, the absorption spectrum of the blend acceptor film (20 wt% L8BO-2O in Y6) shows a low-intensity shoulder peak at 675 nm (Fig. S15 ESI†), which indicate the addition of L8BO-2O could suppress the excessive aggregation of host acceptor. Furthermore, we measured the temperature dependent absorption spectra for Y6, L8BO-2O, and the mixed acceptor (20 wt% L8BO-2O in Y6) dilute solutions, respectively (Fig. S16 ESI†). With temperature increasing, all absorption peaks exhibit a significant blue shift and the extinction coefficient decreases, indicating that the aggregation is disrupted. As shown in Figure S18d-f, after introducing L8BO-2O, the absorption of Y6: L8BO-2O mixed solution showed more significant changes in peak position and intensity compared with the corresponding films, which indicate that the intermolecular interaction between well miscible L8BO-2O and the host Y6 not only slows down the aggregation of Y6, but also leaves space for the ordered stacking of molecules.

To further investigate the miscibility between PM6, Y6 and L8BO-2O, the contact angles of water (H_2O) and diiodomethane (CH_2I_2) droplets on neat films were evaluated, as presented in Fig. 1d. The surface energy (γ_s) and Flory-Huggins interaction parameter (χ) calculated from the equation $\chi = k(\sqrt{\gamma_1}-\sqrt{\gamma_2})^2$are summarized in Table S2 (ESI†).[37, 38] The γ_s values of PM6, Y6 and L8BO-

View Article Online
DOI: 10.1039/D4TC03192J

2O are 32.8, 40.5 and 41.5 mN m^{-1}, respectively. The χ_s values of PM6/Y6 and PM6/L8BO-2O are 0.406 k and 0.505 k, while the χ_s between Y6 and L8BO-2O is only 0.005 k. Similar surface energy and smaller χ suggest good miscibility between Y6 and L8BO-2O.[39, 40] To further verify the good miscibility of two acceptors, the γ_s of blend acceptors films with different proportions were also calculated, as shown in Fig. S17 (ESI†). It can be observed that the γ_s of the mixed acceptors are between that of the two acceptors and are approximately linear correlations with the proportion, which indicates good miscibility between host and guest materials, facilitating the morphology control of mixed films.

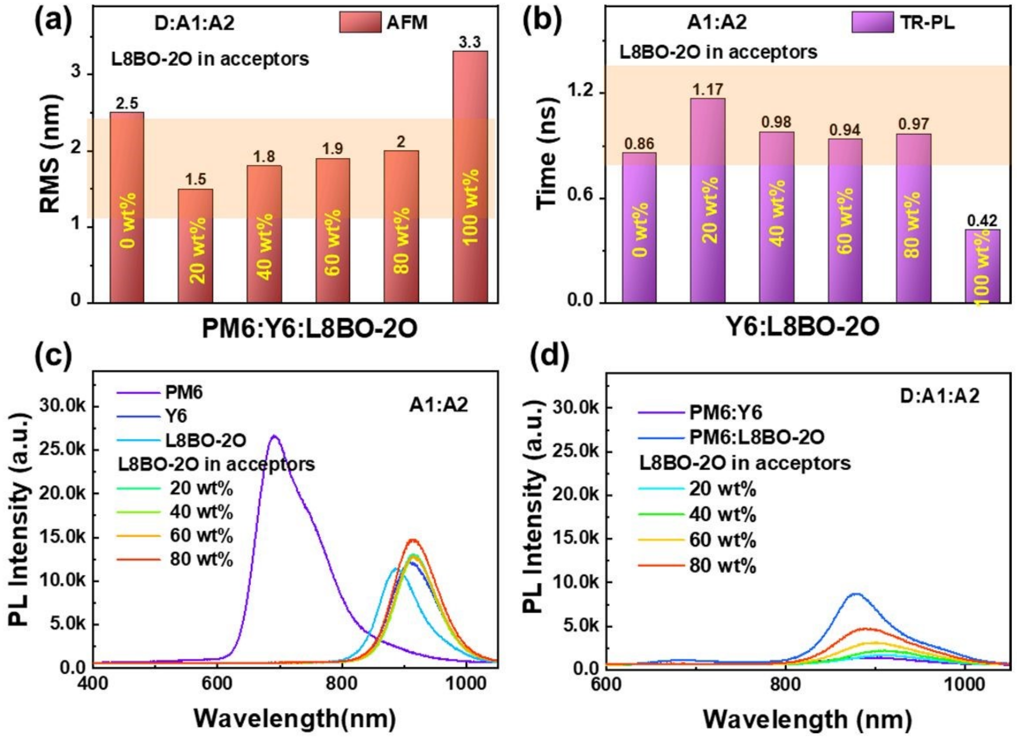

Fig. 2 (a) RMS surface roughness values of PM6:Y6:L8BO-2O blend films with different L8BO-2O contents. (b) Exciton lifetimes of Y6, L8BO-2O and mixed acceptor films. (c) PL spectra of PM6, Y6, L8BO-2O neat films and mixed acceptor films. (d) PL spectra of binary and ternary blend films.

To investigate the morphology characteristic of the ternary active layer after the introduction of L8BO-2O acceptor with good miscibility, atomic force microscopy (AFM) was used. The AFM images are shown in Fig. S18 (ESI†), and the corresponding root-mean-square (RMS) surface roughness values are summarized in Fig. 2a. Both trace and high proportions of third component doping can significantly reduce the roughness of the ternary blend film, which is beneficial for reducing trap defects in the active layer and enhancing the interaction between the host and guest

View Article Online
DOI: 10.1039/D4TC03192J

acceptor molecules, and indicating that L8BO-2O can inhibit the aggregation degree of molecules during the film-formation process in high boiling point solvents.

To understand the working mechanism of L8BO-2O in blend system, time-resolved PL (TR-PL) spectra of neat and mixed acceptors films were measured, as shown in Fig. S19 (ESI†), and the fitted exciton lifetimes are summarized in Fig. 2b. Significantly, all mixed acceptors exhibit longer exciton lifetimes, which can provide sufficient time for exciton diffusion and dissociation. In addition, the steady-state PL spectra of neat and mixed acceptor films are presented in Fig. 2c. The PL peak of Y6 and L8BO-2O neat films are located at 912 and 886 nm, respectively. After adding different ratios of L8BO-2O, the PL intensity of Y6:L8BO-2O blend films shows a slight increase, but the peak position is still the same as Y6 neat film. This phenomenon is typically explained as the energy transfer from L8BO-2O to Y6, through which the light capture achieves optimization.[41-43] The steady-state PL spectra of binary and ternary blend films were also measured, as displayed in Fig. 2d. The PL intensity of all blend films has significantly decreased compared to the neat films, which indicates the occurrence of effective exciton dissociation in the blend films. However, surprisingly, the PL peak position varies with the proportion of the three components in the ternary blend films, which is inconsistent with the pattern presented in the dual acceptor films. This movement of peak position may indicate the presence of additional alloy working mechanisms between L8BO-2O and Y6, which corresponds to the formation of L8BO-2O and Y6 alloy phases due to their good miscibility. To verify this point, it is necessary to further evaluate the photovoltaic performances of the device.

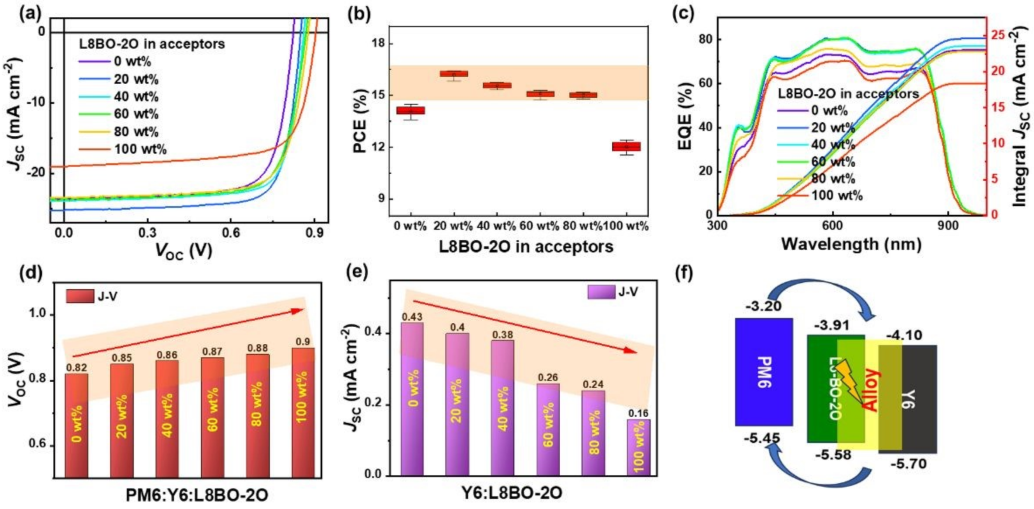

Fig. 3 (a) *J-V* curves, (b) device efficiency statistics obtained from ten devices, (c) the corresponding

View Article Online
DOI: 10.1039/D4TC03192J

EQE spectra and (d) V_{OC}s of PM6:Y6:L8BO-2O based OSCs with different L8BO-2O contents. (e) the *J-V* curves of Y6, L8BO-2O and Y6:L8BO-2O based pure acceptor devices. (f) Schematic diagram of the working mechanism.

Table 1 Photovoltaic parameters of the PM6:Y6:L8BO-2O based OSCs with different L8BO-2O contents.

L8BO-2O in acceptors	V_{OC} (V)	J_{SC} (mA cm^{-2})	J_{SC} (Integral) (mA cm^{-2})	FF (%)	PCE^a (%)
0 wt%	0.82	23.66	22.99	74.71	14.54
	(0.81±0.01)	(22.3±1.4)		(72.5±2.2)	(14.08±0.4)
20 wt%	0.85	25.21	24.62	76.66	16.40
	(0.84±0.01)	(23.8±1.5)		(74.9±1.7)	(16.21±0.2)
40 wt%	0.86	23.89	23.57	76.54	15.75
	(0.85±0.01)	(22.5±1.3)		(74.6±2.0)	(15.56±0.2)
60 wt%	0.87	23.72	22.80	74.05	15.26
	(0.86±0.01)	(22.6±1.1)		(71.8±2.2)	(15.07±0.18)
80 wt%	0.88	23.45	22.78	73.89	15.19
	(0.87±0.01)	(22.2±1.2)		(71.7±2.1)	(15.01±0.15)
100 wt%	0.90	19.00	18.40	72.3	12.42
	(0.89±0.01)	(17.7±1.3)		(70.1±2.2)	(12.01±0.4)

^{a}Average and standard deviation data in parentheses are obtained from ten devices.

To investigate the impact of L8BO-2O on the photovoltaic performance of devices, all binary and ternary OSCs were fabricated based on a conventional device structure of ITO/PEDOT:PSS/active layer/PDINN/Ag. The detailed parameters of the optimization process of OSCs are shown in Fig. S20 and Table S3 (ESI†). The current density-voltage (*J-V*) curves of PM6:Y6 based OSCs with different L8BO-2O contents are shown in Fig. 3a, and the corresponding photovoltaic parameters are summarized in Table 1. The PM6:Y6 based binary OSC exhibits an advanced PCE of 14.54%, with a J_{SC} of 23.66 mA cm^{-2}, a V_{OC} of 0.82 V and an FF of 74.71%. While for PM6:L8BO-2O based binary OSC, a PCE of 12.42%, with a J_{SC} of 19.00 mA cm^{-2}, a V_{OC} of 0.90 V and an FF of 72.3% is delivered. Generally, the content of the third component in the ternary OSCs does not exceed 20%, which is determined by the low mixing tolerance of the selected active layer materials with different physical characteristics. A larger proportion of the third component will lead to a sharp decline in device performance. However, whether a small or a large proportion of the third component is added, the performance of the ternary OSCs has been significantly improved compared to the corresponding binary OSCs. This high mixing tolerance ensures better repeatability of the device's photovoltaic performance (Fig. 3b). When adding 20 wt% L8BO-2O in acceptors,

View Article Online
DOI: 10.1039/D4TC03192J

the optimal ternary OSC achieved the highest PCE of 16.4%, with a much superior J_{SC} of 25.21 mA cm^{-2}, a V_{OC} of 0.85 V, and an FF of 76.66%. Then the external quantum efficiency (EQE) was measured to further explore the reason for the improved J_{SC}, and the EQE spectra of the binary and ternary OSCs are depicted in Fig. 3c. In comparison, all the ternary devices with L8BO-2O exhibited an enhanced EQE response in the visible region, which indicates the absorption of the ternary blends are more efficiently converted to photocurrents. Slight differences between the absorption and EQE spectra are mainly due to the diffraction effect and the interference effect between the incident light and the reflected light from the Ag electrode in the active layers. The integrated J_{SC} from the EQE spectra matches well with that from the *J*-*V* curves but is slightly lower, which is the reason that the EQE is tested in ambient air without any packaging.

According to the above analysis, the PM6:Y6:L8BO-2O based ternary system may have energy transfer and alloy model working mechanisms simultaneously. To further determine the working mechanism, V_{OC} of PM6:Y6:L8BO-2O based ternary OSCs with different L8BO-2O contents are probed and shown in Fig. 3d. With the introduction and content increase of the L8BO-2O, the V_{OC} increases approximately linearly, indicating the existence of an alloy working mechanism between L8BO-2O and Y6. Then the *J*-*V* curves of L8BO-2O, Y6 and L8BO-2O:Y6 based pure acceptor devices were also measured (Fig. 3e). The J_{SC} of L8BO-2O: Y6 based devices are between those of L8BO-2O/Y6 based devices, indicating that no exciton dissociation occurs between L8BO-2O and Y6. Ultimately, L8BO-2O with good miscibility with Y6 not only forms an alloy phase with Y6, but also exhibits energy transfer from L8BO-2O to Y6 in ternary OSCs. The dual mechanism is illustrated in Fig. 3f. This dual mechanism optimized the exciton dissociation and charge transfer process, thereby significantly improving the photovoltaics performance of ternary OSCs under a wide proportion range of the third component.

To clarify the reasons for the high mixing tolerance of L8BO-2O in improving photovoltaic performance, the photocurrent density (J_{ph}) and effective voltage (V_{eff}) curves of binary and ternary OSCs are provided in Fig. S21 (ESI†), and the parameters are listed in Table S4 (ESI†). The J_{ph} is defined as $J_{ph} = J_L$-J_D, where J_L and J_D represent the current density under illumination and dark conditions, respectively. The V_{eff} is defined as $V_{eff} = V_0$-V, where V_0 is the voltage when $J_{ph} = 0$ mA cm^{-2} and the V is the applied voltage.[44] The saturated photocurrent density (J_{sat}) is approximately equal to J_{ph} when V_{eff} = 1 V. The exciton dissociation efficiency (η_{diss}) and charge collection

View Article Online
DOI: 10.1039/D4TC03192J

efficiency (η_{coll}) can be approximately evaluated by J_{ph}/J_{sat}, where J_{ph} is obtained under open circuit conditions and maximum power output condition, respectively. The calculated η_{diss}/η_{coll} of PM6:Y6 and PM6:L8BO-2O binary OSC are 99.1%/ 87.0% and 98.3%/88.3%, respectively. After adding L8BO-2O, the η_{diss} and η_{coll} of PM6:Y6:L8BO-2O based ternary OSCs were enhanced considerably. The enhanced η_{diss} can be attributed to the optimized the phase separation scale of the active layer by L8BO-2O, and the enhanced η_{coll} is attributed to the construction of more effective alloy-like transport channels. The synergistic enhancement of η_{diss} and η_{coll} in ternary OSC indicates more effective charge generation, charge transfer, and suppression of charge recombination, which are beneficial for improving device J_{SC} and FF.

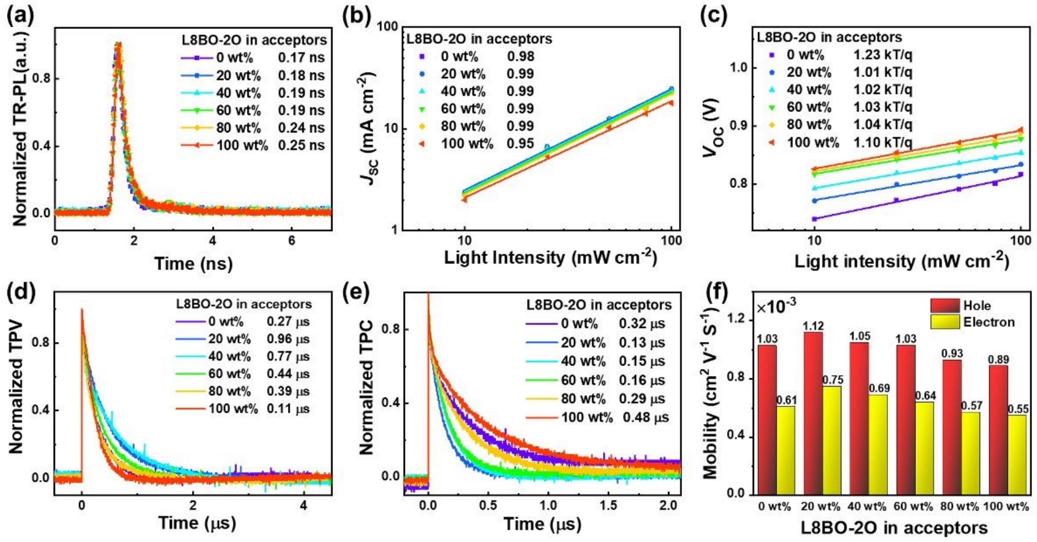

Fig. 4 (a) TR-PL curves of binary and ternary blend films. (b) J_{SC}s and (c) V_{OC}s versus light illumination intensity of the corresponding OSCs. (d) TPV and (e) TPC curves of the corresponding OSCs. (f) Hole and electron mobilities of binary and ternary blend films.

To further verify the improved dissociation efficiency of the device, the TR-PL spectra of binary and ternary blend films are depicted in Fig. 4a. The exciton lifetime (τs) of the PM6:Y6 and PM6:L8BO-2O blend films are 0.17 and 0.25 ns, respectively. After adding L8BO-2O, the τs of ternary blend films significantly decreased, indicating the addition of the third component accelerated the dissociation process of excitons, which is also consistent with the above results. On the other hand, the charge recombination mechanisms of the devices are investigated by fitting the relationship between illumination intensity (P_{light}) and V_{OC}/J_{SC}. The relationship between J_{SC} and P_{light} can be expressed as $J_{SC} \propto P_{light}{}^{s}$. In addition, the relationship between V_{OC} and P_{light} can be expressed as $V_{OC} \propto nkT/q\ln(P_{light})$, where k is the Boltzmann's constant, T is absolute temperature,

View Article Online
DOI: 10.1039/D4TC03192J

and q is the elementary charge. The bimolecular recombination and trap recombination can be ignored when the s or n value approaches 1.00.[45] As shown in Fig. 4b, the s values of the PM6:Y6 based binary and ternary OSCs are more closer to 1.00, indicating the lower bimolecular recombination. Similarly, all the n values of ternary OSCs equal nearly 1.00, indicating the trap recombination of all ternary OSCs has been effectively suppressed compared to PM6:Y6 based binary OSC (Fig. 4c).[46] Lower trap-assisted recombination and bimolecular recombination further explain the significant improvement of FF in the ternary OSCs.

The charge carrier extraction and recombination dynamics were further elucidated by transient photovoltage (TPV) and transient photocurrent (TPC). As shown in Fig. 4d, the fitted carrier lifetimes (τ_{rec}) of ternary OSCs are 0.96 μs (20 wt%), 0.77 μs (40 wt%), 0.44 μs (60 wt%) and 0.39 μs (80 wt%), which are significantly longer than PM6:Y6 (0.27 μs) and PM6:L8BO-2O (0.11 μs) based binary devices. And the fitted charge extraction times (τ_{ext}) of ternary OSCs are 0.13 μs (20 wt %), 0.15 μs (40 wt %), 0.16 μs (60 wt %) and 0.29 μs (80 wt %), which are significantly shorter than PM6:Y6 (0.32 μs) and PM6:L8BO-2O (0.48 μs) based binary devices (Fig. 4e). The results signify that the introduction of L8BO-2O within a wide proportion range can improve charge extraction and suppress charge recombination in the active layer, thereby contributing to achieving more satisfactory J_{SC} and FF.

The hole and electron mobilities were measured by the space charge limited current (SCLC) method. The hole-only and electron-only devices were fabricated with the structure of ITO/PEDOT:PSS/active layer/MoO_3/Ag and ITO/ZnO/active layer/PDINN/Ag. The active layers were prepared under the same conditions as OSCs. The J-V curves of hole-only and electron-only devices were measured in the dark, and the results are shown in Fig. S22 (ESI†). The calculated hole/electron mobilities of PM6:Y6 based device are $1.03\times10^{-3}/0.61\times10^{-3}$ cm^2 V^{-1} S^{-1}. After adding different L8BO-2O contents, the hole/electron mobilities of ternary devices have been increased to $1.12\times10^{-3}/0.75\times10^{-3}$, $1.05\times10^{-3}/0.69\times10^{-3}$, $1.03\times10^{-3}/0.64\times10^{-3}$, $0.93\times10^{-3}/0.57\times10^{-3}$, $0.89\times10^{-3}/0.54\times10^{-3}$ cm^2 V^{-1} S^{-1} for the proportion of 20 wt%, 40 wt %, 60 wt %, 80 wt %, and 100 wt %, respectively, as shown in Fig. 4f. The ratios of $\mu_{\text{h}}/\mu_{\text{e}}$ are listed in Table S5 (ESI†). Faster and more balanced charge transfer in the ternary devices also contribute to the improvement of J_{SC} and PCE.

View Article Online
DOI: 10.1039/D4TC03192J

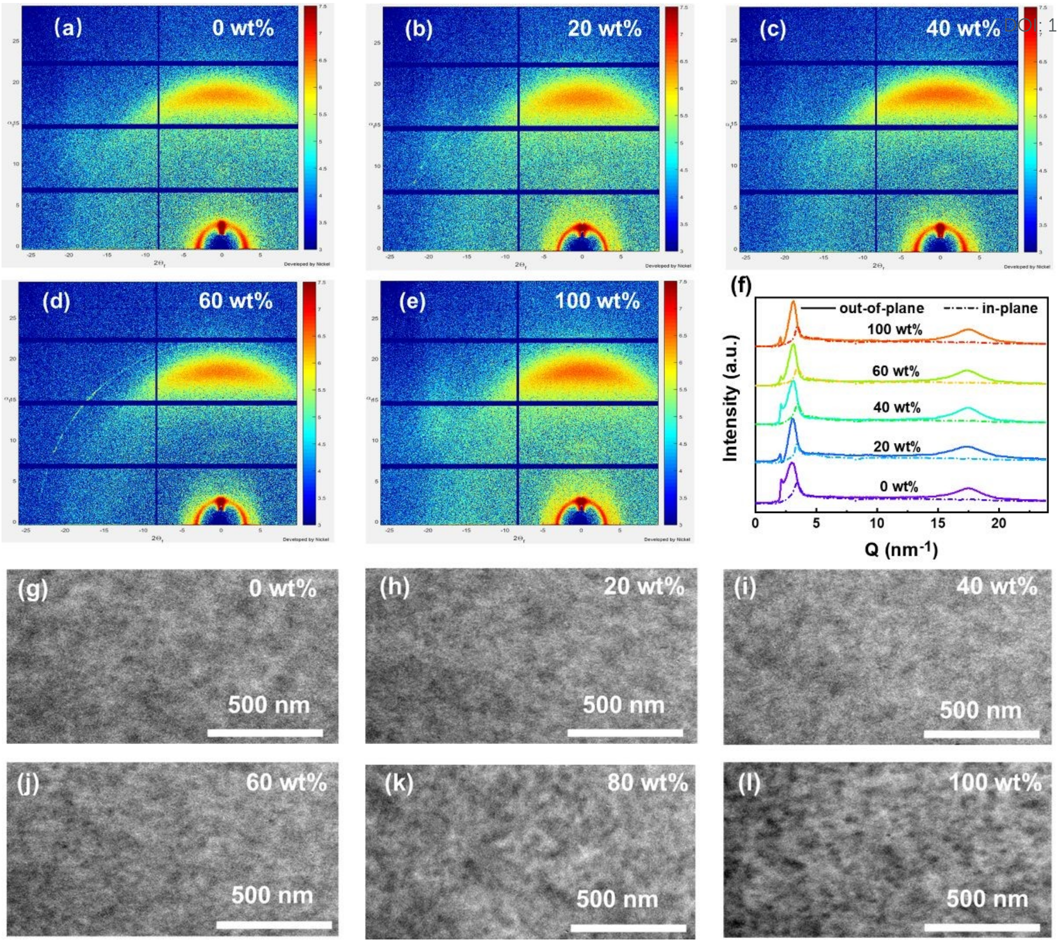

Fig. 5 (a-f) 2D-GIWAXS patterns and corresponding line-cut profiles of binary and ternary blend films. (g-l) TEM images of binary and ternary blend films.

Ordered molecular stacking in the active layer plays an important role in the charge transfer. 2D GIWAXS patterns and line-cut profiles of binary and ternary blend films are shown in Fig. 5a-f, and the corresponding parameters are listed in Table S6 (ESI†). In addition, 2D-GIWAXS patterns of PM6, Y6 and L8BO-2O neat films are shown in Fig. S23 (ESI†). It can be seen that all blend films exhibit a face on/edge on mixed orientation. After adding the third component, the PM6:Y6:L8BO-2O ternary blend films exhibit slightly enhanced out-of-plane (OOP) 010 peaks, indicating enhanced π-π stacking of molecules. It is noteworthy that all binary and ternary films exhibit very similar stacking distances (3.60 Å). The similar geometry structures and intermolecular stacking distances of the two selected acceptors once again confirm their good miscibility, which is conducive to constructing more effective interactions mode between the third component and host system. Furthermore, the crystal coherence length (CCL)[47] calculated from the (010) peak of OOP direction for blend films is 29.09 Å (0 wt%), 31.75 Å (20 wt%), 31.23 Å (40 wt%), 30.39 Å (60 wt%), and 28.96 Å (100 wt%), respectively. The strengthened π-π stacking and increased CCLs are

View Article Online
DOI: 10.1039/D4TC03192J

beneficial for charge transfer and extraction in ternary devices.

The transmission electron microscopy (TEM) images of the binary and ternary blend films are shown in Fig. 5g-l. Compared to the host PM6:Y6 system, the PM6:L8BO-2O blend films exhibit larger phase separation. As discussed above, the good miscibility, similar structure and stacking distance between Y6 and L8BO-2O allow L8BO-2O to blend well into the PM6:Y6 mixture. As shown in the TEM images, the ternary blend films exhibit a similar morphology to the PM6:Y6 host system, even if the third component reaches 80 wt% in acceptors. This harmonious stacking distribution is very conducive to the synergistic effect of the two acceptors in the active layer to achieve more effective photoelectric conversion.

Conclusion

In this work, we designed and synthesized a novel non-fullerene acceptor L8BO-2O with an alkoxy chain as the third component, which can effectively suppress the aggregation effect of the active materials (PM6:Y6) and promote its appropriate phase separation during the film formation process in high boiling point solvents. Meanwhile, the harmonious stacking constructed by the similar structure and stacking distance between L8BO-2O and Y6 promotes more efficient energy transfer and alloy model working mechanism, and significantly increases mixing tolerance. As a result, with the doping of 20 wt% L8BO-2O, the efficiency of champion ternary OSCs reached 16.4%. And within the wide doping range of L8BO-2O (0-80 wt%), the performance of all ternary OSCs is significantly improved. The introduction of a high mixed tolerant third component, which can inhibit molecular aggregation, not only effectively improves the performance of OSCs in high boiling point solvents, but also significantly reduces the difficulty of device manufacturing and increases repeatability of devices.

Conflicts of interest

The authors declare no competing interests.

Supporting Information

Supplemental information can be found in another upload file.

Acknowledgements

The authors are deeply grateful to the National Natural Science Foundation of China (No. 62305350 and 22375213), the Youth Innovation Promotion Association CAS (2021211), Shandong Energy

Institute (SEIS202108, SEII202111), QIBEBT/SEI/QNESL S202305, Shandong postdoctoral innovative talents support plan (SDBX2022031) and Qingdao Postdoctoral Application Research Project (QDBSH20220202026) for financial support. The authors appreciate the beamline BL16B1 of the Shanghai Synchrotron Radiation Facility for providing beam time.

References

1. T. R. Andersen, H. F. Dam, M. Hösel, M. Helgesen, J. E. Carlé, T. T. Larsen-Olsen, S. A. Gevorgyan, J. W. Andreasen, J. Adams, N. Li, F. Machui, G. D. Spyropoulos, T. Ameri, N. Lemaître, M. Legros, A. Scheel, D. Gaiser, K. Kreul, S. Berny, O. R. Lozman, S. Nordman, M. Välimäki, M. Vilkman, R. R. Søndergaard, M. Jørgensen, C. J. Brabec and F. C. Krebs, *Energy Environ. Sci.*, 2014, **7**, 2925-2933.
2. W. Huang, Z. Jiang, K. Fukuda, X. Jiao, C. R. McNeill, T. Yokota and T. Someya, *Joule*, 2020, **4**, 128-141.
3. M. Kaltenbrunner, M. S. White, E. D. Głowacki, T. Sekitani, T. Someya, N. S. Sariciftci and S. Bauer, *Nat. Commun.*, 2012, **3**, 770.
4. F. C. Krebs, *Sol. Energy Mater. Sol. Cells*, 2009, **93**, 394-412.
5. H. Yu, J. Wang, Q. Zhou, J. Qin, Y. Wang, X. Lu and P. Cheng, *Chem. Soc. Rev.*, 2023, **52**, 4132-4148.
6. J. Wang, C. Han, S. Wen, F. Bi, Z. Hu, Y. Li, C. Yang, X. Bao and J. Chu, *Energy Environ. Sci.*, 2023, **16**, 2327-2337.
7. Y. Lin, J. Wang, Z. Zhang, H. Bai, Y. Li, D. Zhu and X. Zhan, *Adv. Mater.*, 2015, **27**, 1170-1174.
8. J. Yuan, T. Huang, P. Cheng, Y. Zou, H. Zhang, J. L. Yang, S. Chang, Z. Zhang, W. Huang, R. Wang, D. Meng, F. Gao and Y. Yang, *Nat. Commun.*, 2019, **10**, 570.
9. J. Fu, Q. Yang, P. Huang, S. Chung, K. Cho, Z. Kan, H. Liu, X. Lu, Y. Lang, H. Lai, F. He, P. W. K. Fong, S. Lu, Y. Yang, Z. Xiao and G. Li, *Nat. Commun.*, 2024, **15**, 1830.
10. Y. Sun, L. Wang, C. Guo, J. Xiao, C. Liu, C. Chen, W. Xia, Z. Gan, J. Cheng, J. Zhou, Z. Chen, J. Zhou, D. Liu, T. Wang and W. Li, *J. Am. Chem. Soc.*, 2024, **146**, 12011-12019.
11. C. Han, J. Wang, S. Zhang, L. Chen, F. Bi, J. Wang, C. Yang, P. Wang, Y. Li and X. Bao, *Adv. Mater.*, 2023, **35**, 2208986.
12. J. Wang, Q. Luan, P. Wang, C. Han, F. Bi, C. Yang, Y. Li and X. Bao, *Adv. Funct. Mater.*, 2023, **33**, 2301575.
13. D. Lee, C. Oh, J. Ryu, S. Jang, I. Hwang and S. Cho, *Mater. Adv.*, 2023, **4**, 4869-4876.
14. L. Zhu, M. Zhang, G. Zhou, T. Hao, J. Xu, J. Wang, C. Qiu, N. Prine, J. Ali, W. Feng, X. Gu, Z. Ma, Z. Tang, H. Zhu, L. Ying, Y. Zhang and F. Liu, *Adv. Energy Mater.*, 2020, **10**, 1904234.
15. X. Dong, Y. Jiang, L. Sun, F. Qin, X. Zhou, X. Lu, W. Wang and Y. Zhou, *Adv. Funct. Mater.*, 2022, **32**, 2110209.
16. Y. Cui, H. Yao, J. Zhang, K. Xian, T. Zhang, L. Hong, Y. Wang, Y. Xu, K. Ma, C. An, C. He, Z. Wei, F. Gao and J. Hou, *Adv. Mater.*, 2020, **32**, 1908205.
17. K. Jiang, Q. Wei, J. Y. L. Lai, Z. Peng, H. K. Kim, J. Yuan, L. Ye, H. Ade, Y. Zou and H. Yan, *Joule*, 2019, **3**, 3020-3033.

View Article Online
DOI: 10.1039/D4TC03192J

18. W. Zhao, S. Li, H. Yao, S. Zhang, Y. Zhang, B. Yang and J. Hou, *J. Am. Chem. Soc.*, 2017, **139**, 7148-7151.

19. P. Wang, F. Bi, Y. Li, C. Han, N. Zheng, S. Zhang, J. Wang, Y. Wu and X. Bao, *Adv. Funct. Mater.*, 2022, **32**, 2200166.

20. M. Liu, X. Ge, X. Jiang, F. Guo, S. Gao, Q. Peng, L. Zhao and Y. Zhang, *Adv. Funct. Mater.*, 2023, **33**, 2300214.

21. J. Lv, H. Tang, J. Huang, C. Yan, K. Liu, Q. Yang, D. Hu, R. Singh, J. Lee, S. Lu, G. Li and Z. Kan, *Energy Environ. Sci.*, 2021, **14**, 3044-3052.

22. Z. Zheng, E. He, J. Wang, Z. Qin, T. Niu, F. Guo, S. Gao, Z. Ma, L. Zhao, X. Lu, Q. Xue, Y. Cao, G. T. Mola and Y. Zhang, *J. Mater. Chem. A*, 2021, **9**, 26105-26112.

23. L. Zhong, Z. Sun, S. Lee, S. Jeong, S. Jung, Y. Cho, J. Park, J. Park, S. Yoon and C. Yang, *Adv. Funct. Mater.*, 2023, **33**, 2305450.

24. C. Yang, M. Jiang, S. Wang, B. Zhang, P. Mao, H. Y. Woo, F. Zhang, J. Wang and Q. An, *Adv. Mater.*, 2024, **36**, 2305356.

25. H. Chen, R. Zhang, X. Chen, G. Zeng, L. Kobera, S. Abbrent, B. Zhang, W. Chen, G. Xu, J. Oh, S.-H. Kang, S. Chen, C. Yang, J. Brus, J. Hou, F. Gao, Y. Li and Y. Li, *Nat. Energy*, 2021, **6**, 1045-1053.

26. J. Wang, C. Han, J. Han, F. Bi, X. Sun, S. Wen, C. Yang, C. Yang, X. Bao and J. Chu, *Adv. Energy Mater.*, 2022, **12**, 2201614.

27. M. Liu, X. Ge, X. Jiang, D. Chen, F. Guo, S. Gao, Q. Peng, L. Zhao and Y. Zhang, *Nano Energy*, 2023, **112**, 108501.

28. H. Chen, W. Sun, R. Zhang, Y. Huang, B. Zhang, G. Zeng, J. Ding, W. Chen, F. Gao, Y. Li and Y. Li, *Adv. Mater.*, 2024, **36**, 2402350.

29. Y. Huang, H. Chen, Q. Fan, Z. Chen, J. Ding, H. Yang, Z. Sun, R. Zhang, W. Chen, C. Yang, F. Gao and Y. Li, *Chin. J. Chem.*, 2023, **41**, 1066-1074.

30. Q. An, F. Zhang, J. Zhang, W. Tang, Z. Deng and B. Hu, *Energy Environ. Sci.*, 2016, **9**, 281-322.

31. N. Gasparini, X. Jiao, T. Heumueller, D. Baran, G. J. Matt, S. Fladischer, E. Spiecker, H. Ade, C. J. Brabec and T. Ameri, *Nat. Energy*, 2016, **1**, 16118.

32. Y. Li, Y. Cai, Y. Xie, J. Song, H. Wu, Z. Tang, J. Zhang, F. Huang and Y. Sun, *Energy Environ. Sci.*, 2021, **14**, 5009-5016.

33. J. Wang, C. Han, F. Bi, D. Huang, Y. Wu, Y. Li, S. Wen, L. Han, C. Yang, X. Bao and J. Chu, *Energy Environ. Sci.*, 2021, **14**, 5968-5978.

34. J. Wang, Y. Li, C. Han, L. Chen, F. Bi, Z. Hu, C. Yang, X. Bao and J. Chu, *Energy Environ. Sci.*, 2024, **17**, 4216-4227.

35. L. Zhan, S. Li, T. Lau, Y. Cui, X. Lu, M. Shi, C. Li, H. Li, J. Hou and H. Chen, *Energy Environ. Sci.*, 2020, **13**, 635-645.

36. C. Zhang, X. Zhong, X. Sun, J. Lv, Y. Ji, J. Fu, C. Zhao, Y. Yao, G. Zhang, W. Deng, K. Wang, G. Li and H. Hu, *Adv. Sci.*, 2024, **11**, 2401313.

37. S. Nilsson, A. Bernasik, A. Budkowski and E. Moons, *Macromolecules*, 2007, **40**, 8291-8301.

38. J. Comyn, *Int. J. Adhes. Adhes.*, 1992, **12**, 145-149.

39. K.-H. Kim, H. Kang, H. J. Kim, P. S. Kim, S. C. Yoon and B. J. Kim, *Chem. Mater.*, 2012, **24**, 2373-2381.

40. Y. Cai, Y. Li, R. Wang, H. Wu, Z. Chen, J. Zhang, Z. Ma, X. Hao, Y. Zhao, C. Zhang, F. Huang

View Article Online
DOI: 10.1039/D4TC03192J

and Y. Sun, *Adv. Mater.*, 2021, **33**, 2101733.

41. S. Karuthedath, J. Gorenflot, Y. Firdaus, N. Chaturvedi, C. S. P. De Castro, G. T. Harrison, J. I. Khan, A. Markina, A. H. Balawi, T. A. D. Peña, W. Liu, R. Liang, A. Sharma, S. H. K. Paleti, W. Zhang, Y. Lin, E. Alarousu, S. Lopatin, D. H. Anjum, P. M. Beaujuge, S. De Wolf, I. McCulloch, T. D. Anthopoulos, D. Baran, D. Andrienko and F. Laquai, *Nat. Mater.*, 2021, **20**, 378-384.
42. J.-S. Huang, T. Goh, X. Li, M. Y. Sfeir, E. A. Bielinski, S. Tomasulo, M. L. Lee, N. Hazari and A. D. Taylor, *Nat. Photonics*, 2013, **7**, 479-485.
43. S. Karuthedath, Y. Firdaus, R. Liang, J. Gorenflot, P. M. Beaujuge, T. D. Anthopoulos and F. Laquai, *Adv. Energy Mater.*, 2019, **9**, 1901443.
44. P. W. M. Blom, V. D. Mihailetchi, L. J. A. Koster and D. E. Markov, *Adv. Mater.*, 2007, **19**, 1551-1566.
45. A. K. K. Kyaw, D. H. Wang, V. Gupta, W. L. Leong, L. Ke, G. C. Bazan and A. J. Heeger, *ACS Nano*, 2013, **7**, 4569-4577.
46. L. J. A. Koster, V. D. Mihailetchi, R. Ramaker and P. W. M. Blom, *Appl. Phys. Lett.*, 2005, **86**, 123509.
47. D. M. Smilgies, *J. Appl. Crystallogr.*, 2009, **42**, 1030-1034.

View Article Online
DOI: 10.1039/D4TC03192J

Data Availability Statement

The data that supports the finding of this study are available in the supplementary material of this article or from the corresponding authors upon reasonable request.